Available online at www.sciencedirect.com
ScienceDirect
Journal of Theoretical Biology 244 (2007) 553–564
Journal of Theoretical Biology
www.elsevier.com/locate/yjtbi

A mathematical model for adaptive transport network in path finding by true slime mold

Atsushi Tero[a,*], Ryo Kobayashi[a], Toshiyuki Nakagaki[b,c]

[a]*Department of Mathematical and Life Sciences, Hiroshima University, Higashi Hiroshima 739-8526, Japan*
[b]*Research Institute for Electronic Science, Hokkaido University, Sapporo, 060-0812, Japan*
[c]*Creative Research Initiative "SOUSEI", Hokkaido University, Sapporo, 001-0021, Japan*

Received 7 October 2005; received in revised form 3 July 2006; accepted 6 July 2006
Available online 24 July 2006

Abstract

We describe here a mathematical model of the adaptive dynamics of a transport network of the true slime mold *Physarum polycephalum*, an amoeboid organism that exhibits path-finding behavior in a maze. This organism possesses a network of tubular elements, by means of which nutrients and signals circulate through the plasmodium. When the organism is put in a maze, the network changes its shape to connect two exits by the shortest path. This process of path-finding is attributed to an underlying physiological mechanism: a tube thickens as the flux through it increases. The experimental evidence for this is, however, only qualitative. We constructed a mathematical model of the general form of the tube dynamics. Our model contains a key parameter corresponding to the extent of the feedback regulation between the thickness of a tube and the flux through it. We demonstrate the dependence of the behavior of the model on this parameter.

Keywords: *Physarum polycephalum*; Mathematical modeling; Natural adaptive networks

1. Introduction

There are two fundamental questions regarding information processing in a biological system: Firstly, how "smart" is an organism? Secondly, how does the organism realize this smartness? Even unicellular organisms can demonstrate a greater capacity than initially thought for processing information, for example by solving a maze (Nakagaki et al., 2000a; Nakagaki, 2001; Nakagaki et al., 2004a,b). Here we provide an answer to the question of how the amoeboid true slime mold, *Physarum polycephalum*, realized this capacity. This organism is useful for study of biological information processing, since the simplicity and homogeneity of its body structure assist in the preparation of mathematical models.

The body of the plasmodium of *P. polycephalum* contains a network of tubes, by means of which nutrients and chemical signals circulate throughout the organism (Nakagaki et al., 2000a; Nakagaki, 2001). Circulation is based on streaming through a complicated network of tubular channels (TCs). Thus, the geometry of the tube network is related to the transport of materials and information within the organism. Since the tubes disassemble and reassemble within a period of a few hours in response to external conditions, this system is very useful for studying the function and dynamics of natural adaptive networks (Nakagaki et al., 2004a,b).

When food sources (FSs) were presented to a starved plasmodium that was spread over the entire agar surface, regions of the plasmodium concentrated at each FS, as shown in Fig. 1. Almost the entire plasmodium was taken up in this accumulation, covering each source in order to absorb nutrients, and only a few tubes remained connecting the separated components of the plasmodium. It should be noted that the connecting path traced the shortest route to the FSs even in the complex geometry of a maze (Nakagaki et al., 2000a, 2001). This phenomenon can be applied to both path-finding in a maze and path selection in a transport network. It is difficult to develop a

*Corresponding author. Tel.: +81 11 706 9243.
E-mail address: tero@topology.coe.hokudai.ac.jp (A. Tero).

0022-5193/$ - see front matter © 2006 Elsevier Ltd. All rights reserved.
doi:10.1016/j.jtbi.2006.07.015

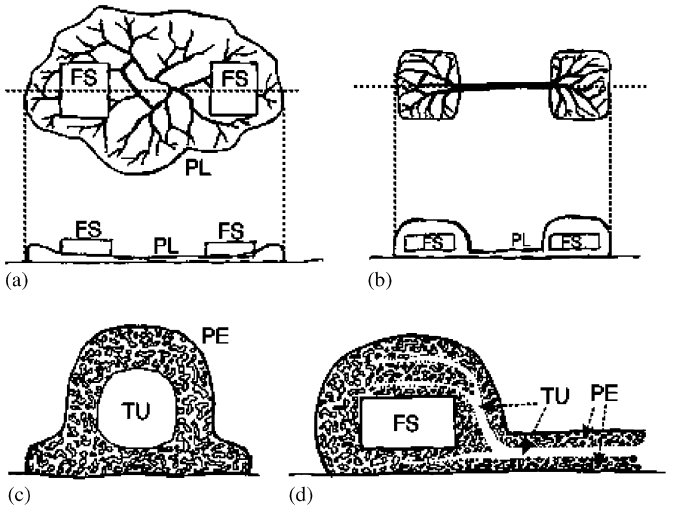

Fig. 1. Schematic illustration of the changes in cell structure in response to food. At first the plasmodium (PL) has a quasi-elliptic shape and the food sources (FSs) are placed on the PL at two locations (a). The plasmodium then gathers around the FSs, connecting them via a thick tube. The shape resembles a dumbbell (b). The panel (c) gives a cross-sectional view of the thick tube shown in (b). The sol flows through the tubular channels (TU), which are made up of the actin-myosin fibers (PE or sponge part). The actin-myosin fibers around the FSs exhibits rhythmic contractions and push the sol into the tube (d).

mathematical algorithm describing this natural form of computation, because it is not known how the amoeboid organism tackles this sort of combinatorial optimization problem.

Since the driving force for transportation is the variation in hydrostatic pressure along the tube, the hydrodynamic theory implies that thick, short tubes are, in principle, the most effective for transportation (Kamiya, 1959). By forming the thickest, shortest tubes, the organism optimizes its task of survival for the following reasons: (1) the area of its body lying over the FS and working to absorb nutrients is maximized and (2) intracellular communication via the exchange of chemical signals between the positions of FSs is at its most effective. Hence, this rather smart strategy implies that the plasmodium is capable of solving complex problems. In order to investigate the mechanisms by which the path finding is achieved, we have developed a mathematical model to simulate the adaptive dynamics of tube networks.

2. Physiological background

Two empirical rules describe changes in the tubular structure of the plasmodium: first, open-ended tubes, which are not connected to a FS, tend to disappear; second, when two or more tubes connect the same two FSs, the longer tubes tend to disappear (Nakagaki et al., 2001). These changes are closely related to the spatio-temporal dynamics of cellular rhythms, as described below.

Tubular structures are formed in a specific direction when shuttle streaming of the protoplasm, driven by hydrostatic pressure due to rhythmic contractions, persists in that direction for a certain period (Nakagaki et al., 2000b). This experimental result can be explained at the molecular level. Actomyosin fibers are arranged along the length of the cortex of a tube, forming the basic framework of the tube (Naib-Majani et al., 1982; Stockem and Brix, 1994). A similar kind of fiber orientation is induced by artificial stretching of plasmodial tissue. This phenomenon is known as the stretch activation effect (Kamiya, 1959; Nagai et al., 1978) and is a natural property of fibrous molecules. For instance, when a sheet made of vinyl chloride is stretched, randomly oriented molecules tend to reorient in the direction of the stretching force. This implies that if there were a stretching force within the organism, it could act to organize the tubular structures. A candidate force is the shear stress exerted by fast flowing (1 mm/s) protoplasm. The estimated magnitude of the shear stress is great enough to produce stretch activation. In summary, then, it can be hypothesized that shear stress exerted by the flow of protoplasm induces the stretching effect, which in turn leads to regular orientation of the actomyosin fibers as the basic framework of the tubes. What does this mean for the regulation of tube formation? The answer lies in positive feedback control between flux and thickness of the tube, as described below.

The plasmodium consists of two parts: a "sponge" section including distributed actin-myosin fibers and a "tube" section made up of actin-myosin fibers. As illustrated in Fig. 1, the protoplasmic sol in the sponge section flows in and out of the tube section.

The tube widens with sufficient flux. This leads to a further increase of flux because the resistance to the flow of sol decreases in the wider channel. Hence, tubes with a large flux grow, while those with a small flux disappear. Clearly this dynamic behavior of the tube diameter is autocatalytic. In other words, the network has the ability to adapt to variations of flux. We therefore included this adaptability in our model. However, since the experimental data are not quantitative but qualitative, there remained a large degree of freedom in formulating the model.

In order to understand the tube dynamics, we have to consider another issue: how is the motive force of protoplasmic flow determined? The actin-myosin fibers in the sponge section exhibit rhythmic contractions with a period of 2 min. These contractions exert pressure on the protoplasmic sol, which makes it flow into the tube, through it, and out at the other end. The flow in the tube is not unidirectional; the direction of flow can be observed to switch back and forth. These periodic changes in direction are known as protoplasmic shuttle streaming.

When FSs are presented to the organism, the oscillations are out of phase between one FS and its neighboring tube. This means that the sol in the FS flows in and out of the tube. When there are two FSs, the two of them push the sol, sometimes in phase and sometimes out of phase. In any case, the sol is exchanged between the two FSs over longer periods of time: even in in-phase oscillation, the sol flows

through the tube between the FSs because baseline and amplitude of pressure oscillation are different from each other. Hence it is reasonable to assume that, at any given moment, one FS is the source and the other the sink of sol flow. Moreover, we assume that only the component of the organism at the FS can generate pressure, and that the tube is a passive element, since most of the organism lies over the FSs and produces mechanical force synchronously at each FS.

There have been many studies of patterns of rhythmic contractions in relation to cell behavior (Matsumoto et al., 1988; Miyake et al., 1996; Takamatsu et al., 2001; Oster and Odell, 1984; Teplov et al., 1991; Takahashi et al., 1997; Tero et al., 2005). However we will not consider this matter further here: instead we propose to shed light on the regulation of tube thickness by flux. Based on the above assumptions, we will clarify the dynamical behavior of the adaptive tube network.

3. Formulation of the mathematical model

Before deriving model equations, let us recall the way in which the plasmodium of *Physarum* solves a maze. The maze is initially filled by the plasmodium as shown in Fig. 2(a); the tubular network then appears, and the tubes in the dead end degenerate (b); finally, the shortest path remains (c). We will adopt this particular maze as an example for our simulations. The conformation of the initial tubular network of the organism is represented by the graph in Fig. 2(d), where each edge of the graph represents a tube segment. The two special nodes

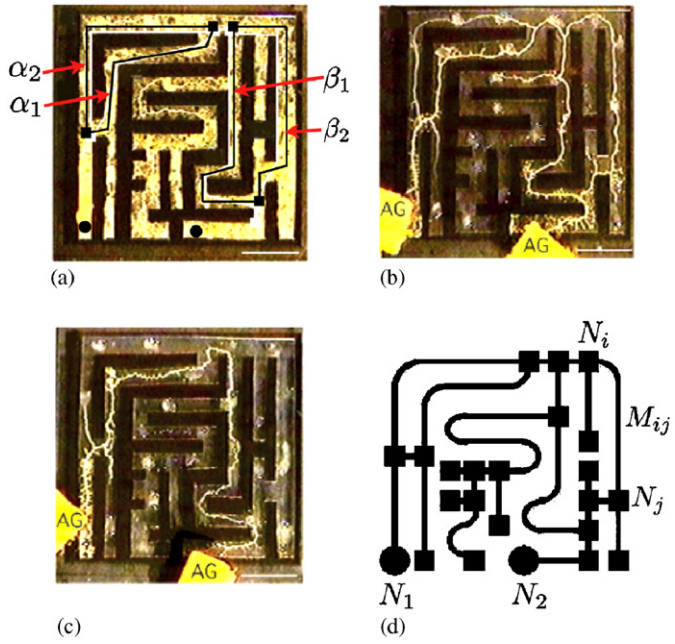

Fig. 2. Panels (a)–(c) illustrate the plasmodial maze-solving process: (a) initial state; (b) intermediate state; (c) final state. Panel (d) is a graphical representation of the maze. The source node N_1 and the sink node N_2 are indicated by solid circles and other nodes are shown by solid squares.

corresponding to the FSs are named N_1 and N_2 and other nodes are designated N_3, N_4, N_5, and so forth. As proposed in the previous section, one of the FS nodes (N_1) always acts as a source and the other (N_2) as a sink. The edge between N_i and N_j is designated M_{ij}. If there are several edges between the same nodes, they are designated M_{ij}^1, M_{ij}^2, and so forth.

3.1. The flux of sol through the tubes

The variable Q_{ij} is used to express the flux through M_{ij} from N_i to N_j. Let us assume that the flow along the tube is approximately Poiseuille flow. The flux Q_{ij} can then be expressed by the formula

$$Q_{ij} = \frac{\pi a_{ij}^4}{8\kappa} \frac{p_i - p_j}{L_{ij}},$$

where L_{ij} and a_{ij} are the length and radius, respectively, of the tube corresponding to the edge M_{ij}, κ is the viscosity coefficient of the sol and p_i is the pressure at the node N_i. By setting $D_{ij} = \pi a_{ij}^4/8\kappa$ what we call the conductivity of the edge M_{ij}, the above equation can be rewritten as

$$Q_{ij} = \frac{D_{ij}}{L_{ij}} (p_i - p_j). \tag{1}$$

We assume zero capacity at each node; hence by considering the conservation law of sol we have

$$\sum_i Q_{ij} = 0 \quad (j \neq 1, 2). \tag{2}$$

For the source node N_1 and the sink node N_2, the following two equations hold

$$\sum_i Q_{i1} + I_0 = 0, \quad \sum_i Q_{i2} - I_0 = 0, \tag{3}$$

where I_0 is the flux flowing from the source node (or into the sink node). It should be noted that I_0 is a constant in our model, which means that the total flux is fixed constant throughout the process.

3.2. Adaptation

Experimental observation shows that tubes with larger fluxes are reinforced, while those with smaller fluxes degenerate. In order to describe such adaptation of tubular thickness we assume that the conductivity D_{ij} changes over time according to the flux Q_{ij}. We propose the following equation for the evolution of $D_{ij}(t)$

$$\frac{\mathrm{d}}{\mathrm{d}t} D_{ij} = f(|Q_{ij}|) - rD_{ij}, \tag{4}$$

where r is a decay rate of the tube. This equation implies that the conductivity tends to vanish if there is no flux along the edge, while it is enhanced by the flux. It is natural to assume that f is a monotonically increasing continuous function satisfying $f(0) = 0$. Note that the edge lengths,

L_{ij}'s are kept constant throughout the adaptation process in contrast to D_{ij}'s.

3.3. Dimensionless model equations

Let us take a characteristic magnitude of flux I_0, and take a characteristic conductivity $\bar{D}$ so that the relation $f(I_0) - r\bar{D} = 0$ holds. By setting $t = (1/r)\tilde{t}$ and $D_{ij} = \bar{D}\tilde{D}_{ij}$ and $Q_{ij} = I_0\tilde{Q}_{ij}$, we have $\mathrm{d}/\mathrm{d}\tilde{t}\tilde{D}_{ij} = \tilde{f}(|\tilde{Q}_{ij}|) - \tilde{D}_{ij}$, where $\tilde{f}(\tilde{Q}) = f(I_0\tilde{Q})/f(I_0)$.

In this paper, we will consider two types of functions $f(Q)$ which are given by $f(Q) = mQ^{\mu}$ and $f(Q) = \delta(Q/Q_h)^{\mu}/1 + (Q/Q_h)^{\mu}$ where the exponent μ is positive. The former $f(Q)$ is a simple choice which is a monotonically increasing continuous function satisfying $f(0) = 0$. The latter $f(Q)$ also satisfies these conditions and saturates where Q_h gives a half of the saturation level. The former $f(Q)$ derives a dimensionless function form $\tilde{f}(\tilde{Q}) = \tilde{Q}^{\mu}$, and the latter $f(Q)$ derives $\tilde{f}(\tilde{Q}) = (1+a)\tilde{Q}^{\mu}/1 + a\tilde{Q}^{\mu}$, where $a = (I_0/Q_h)^{\mu}$. Hereafter, we call the former dimensionless function form Type I, and the latter Type II. Note that Type I function has one parameter μ, while Type II function has two parameters μ and a.

By omitting ˜ from the dimensionless variables and function, we obtain the following dimensionless model equation

$$\frac{\mathrm{d}}{\mathrm{d}t}D_{ij} = f(|Q_{ij}|) - D_{ij}, \tag{5}$$

which we call an *adaptation equation*. Also, the characteristic length $\bar{L}$ is taken to be the shortest edge length, and the characteristic pressure $\bar{p}$ is given by the relation $\bar{p} = I_0\bar{L}/\bar{D}$, and we set $L_{ij} = \bar{L}\tilde{L}_{ij}$ and $p_i = \bar{p}\tilde{p}_i$. Then the network Poisson equation[1] for the pressure is derived from Eqs. (1)–(3) as follows:

$$\sum_i \frac{D_{ij}}{L_{ij}}(p_i - p_j) = \begin{cases} -1 & \text{for } j = 1, \\ +1 & \text{for } j = 2, \\ 0 & \text{otherwise.} \end{cases} \tag{6}$$

Note that ˜ is already omitted in Eq. (6) from each dimensionless variable and constant as performed when obtaining Eq. (5). By setting $p_2 = 0$ as the basic pressure level, all p_i's can be determined by solving the equation system (6), and each $Q_{ij} = D_{ij}/L_{ij}(p_i - p_j)$ is also obtained.

What should be emphasized is how our model expresses the process of evolution. The variable D_{ij}'s evolve according to the adaptation Eq. (5), and variables such as p_i and Q_{ij} are determined by solving the network Poisson equation (6) characterized by the value of the D_{ij}'s (and L_{ij}'s) *at each moment*.

Here we refer to the numerical schemes shortly. The network Poisson equation (6) yields a linear equation system with sparse symmetric matrix which is numerically solved by standard ICCG (Incomplete Cholesky Conjugate Gradient) method. We solved the adaptation equation (5) using a semi-implicit scheme as follows:

$$\frac{D_{ij}^{n+1} - D_{ij}^{n}}{\delta t} = f(|Q_{ij}^{n}|) - D_{ij}^{n+1},$$

where δt is a time mesh size and the upper index n indicates a time step.

The conductivity is closely related to the thickness of the tube. Therefore, the disappearance of tubes is expressed by the extinction of the conductivity of edges. During the evolution of the model system, some edges grow or remain while others disappear. We consider that our system has solved the maze when the remaining edges form a path (or paths) connecting the two special nodes N_1 and N_2.

Because the total flux is kept constant, there is, in a sense, competition between edges—with each scrambling for more flux. It is clear that positive feedback is included in our model equations, since $f(Q)$ is an increasing function. However, it is not easy to predict how the system evolves and what the asymptotic behavior will be for a given function form $f(Q)$ and given parameter values of the parameters, as we will see in the next section.

4. Simulations of maze solving

In this section, we show that the model can solve a maze in a manner similar to that used by the plasmodium of *Physarum*. That is, our system automatically eliminates some edges by reducing their conductivity, and reinforces other edges, to arrive at a solution of the maze. Therefore, we are especially interested in the asymptotic behavior of the system—i.e. which edges survive in the long run.

We will describe simulations using the model equations (5) and (6) adopting Type I function $f(Q) = Q^{\mu}$ and Type II function $f(Q) = (1+a)Q^{\mu}/1 + aQ^{\mu}$. In type II function, the parameter μ is taken in the range $\mu > 1$ to keep the sigmoidal profile as indicated in Fig. 3(b).

The graph presented in Fig. 2(d) is adopted here. The basic structure of the graph is expressed by the list of edges, $\{M_{ij}\}_{i,j}$, and their lengths, $\{L_{ij}\}_{i,j}$, which are fixed throughout the simulation. The path in the graph in Fig. 2(a) corresponding to the real path α_2 has one edge, while the path corresponding to α_1 has two edges. Similarly, the

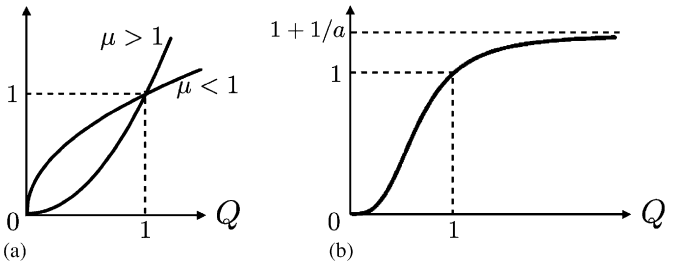

Fig. 3. (a) Illustration of the graph of Type I function $f(Q) = Q^{\mu}$ ($\mu > 0$); (b) illustration of the graph of Type II function $f(Q) = (1+a)Q^{\mu}/1 + aQ^{\mu}$ ($\mu > 1$ and $a > 0$). Note that $f(1) = 1$ holds by definition of dimensionless functions.

[1]Note that the left-hand side of (6) is a non-uniform discrete Laplacian of the pressure p.

paths corresponding to β_1 and β_2 have two and four edges, respectively. Hereafter, we will designate the path in the graph by the name of the real path to which it corresponds, provided that the expression is not confusing. The length of the path in the graph is the sum of the lengths of the edges that compose the path. In our graph, the lengths of four paths α_1, α_2, β_1 and β_2 are set as indicated in the table below. Note that the ratio between the lengths of α_1 and α_2 is greater than the ratio between the lengths of β_1 and β_2.

Path	α_1	α_2	β_1	β_2
Length	15.425	16.500	18.164	19.000
Ratio	1.070		1.046	

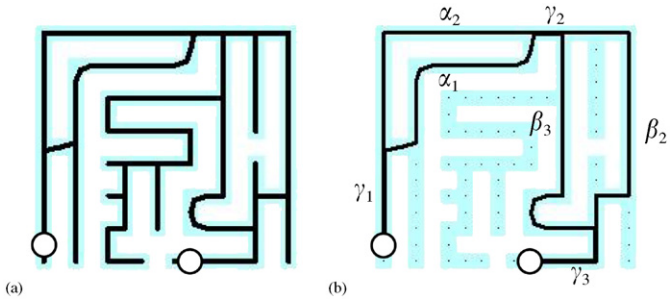

Fig. 4. The thickness of each edge indicates its conductivity, and this procedure is adopted in all subsequent panels of a similar nature: (a) the initial state, and (b) the intermediate state in which the dead end paths have already degenerated, while the paths α_1, α_2, β_1, and β_2 remain. The paths that should be included in the *solution* are designated γ_1, γ_2, and γ_3.

The initial values of D_{ij} are randomly set, which are distributed uniformly within the interval $[0.5, 1.0]$ unless especially noted.

In all the simulations, the dead end paths vanish first; we will refer to this hereafter as *dead end cutting*. Thus the transition from the initial state indicated in Fig. 4(a) to the intermediate state in Fig. 4(b) is always observed. Actually dead end cutting is completed by the time $t = 5$ as will be shown in the left panels of Figs. 5–10. However, there are differences between the asymptotic behaviors for different choice of the function type and parameter values, which will be demonstrated in the following subsections.

4.1. Type I: $f(Q) = Q^{\mu}$

Simulations are shown below for each case: $\mu > 1$, $0 < \mu < 1$, and $\mu = 1$.

Case I: $\mu > 1$. Fig. 5(a) and (c) illustrate the evolution of the system by plotting the conductivities $D_{ij}(t)$ for all edges. Rapid dead end cutting is observed, while the key paths such as γ_1, γ_2, and γ_3 that must be included in the *solution* (see Fig. 4(b)) are reinforced and their conductivities quickly converge to $f(1) = 1$. (Note that dimensionless total flux is always set unity by our non-dimensionalization process.)

After reaching the intermediate form shown in Fig. 4(b), one of the paths α_1 and α_2 and one of the paths β_1 and β_2 are selected at the following stage in this parameter range. If the initial value of D_{ij} is taken as almost uniform, paths α_1 and β_1 always survive, as shown in Fig. 5(a) and (b). However, the path β_2 can remain instead of β_1 as in Fig. 5(c) and (d), if the initial conductivity of the path β_1 is

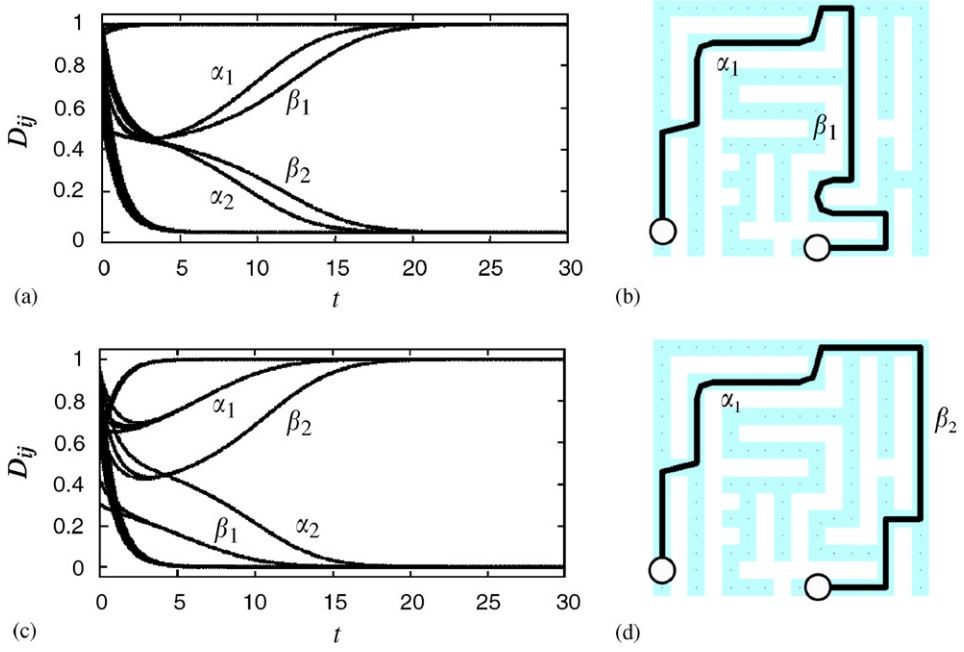

Fig. 5. The parameter is set at $\mu = 1.2$: (a) superimposed plots of D_{ij}'s vs. time; (b) final state corresponding to panel (a); (c) superimposed plots of D_{ij}'s vs. time; (d) final state corresponding to panel (c). The difference between the upper and lower panels derives from the difference in initial states. In the simulation corresponding to the lower panels, initial D_{ij}'s in the path β_1 was set randomly in the interval $[0.25, 0.50]$.

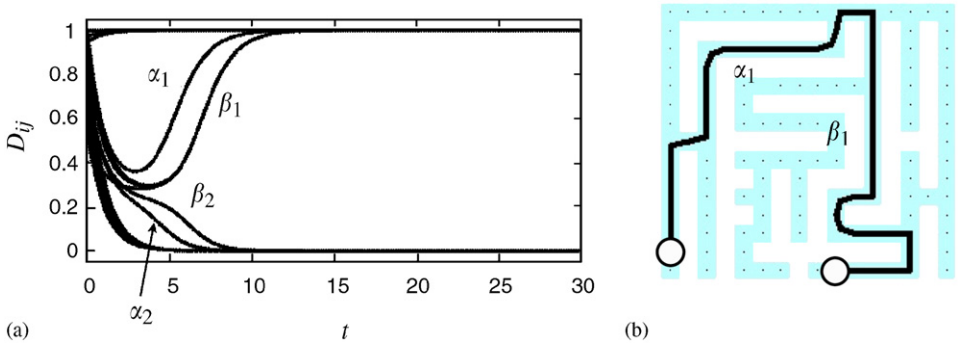

Fig. 6. The parameter is set at $\mu = 2.0$: (a) superimposed plots of time vs. D_{ij}'s; (b) final state.

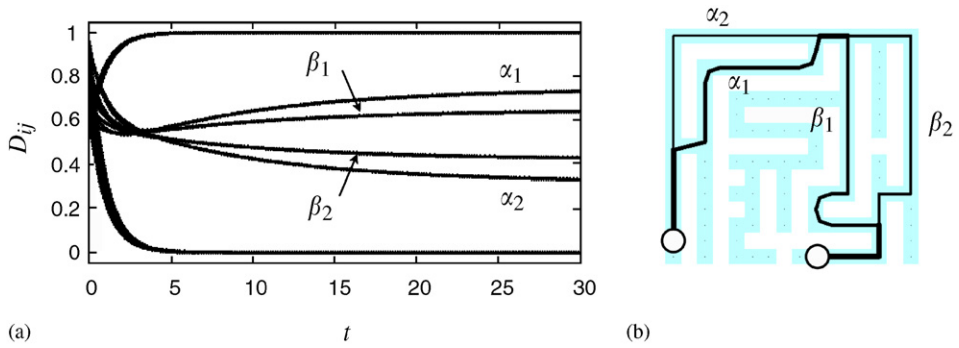

Fig. 7. The parameter is set at $\mu = 0.9$: (a) superimposed plots of D_{ij}'s vs. time; (b) final state.

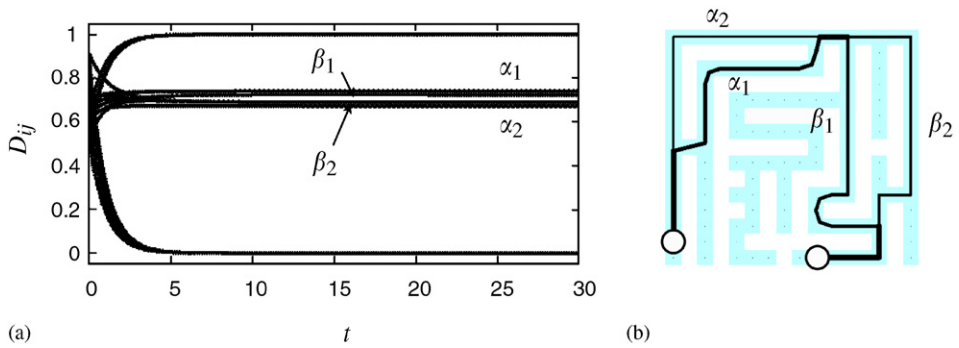

Fig. 8. The parameter is set at $\mu = 0.5$: (a) superimposed plots of D_{ij}'s vs. time; (b) final state.

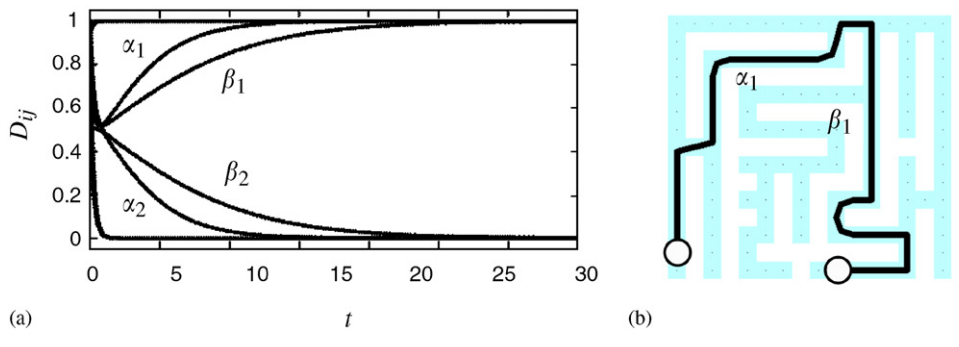

Fig. 9. The parameter is set at $\mu = 1.0$: (a) superimposed plots of D_{ij}'s vs. time; (b) final state. Note that the time-scale in panel (a) is different from that used in the previous figures.

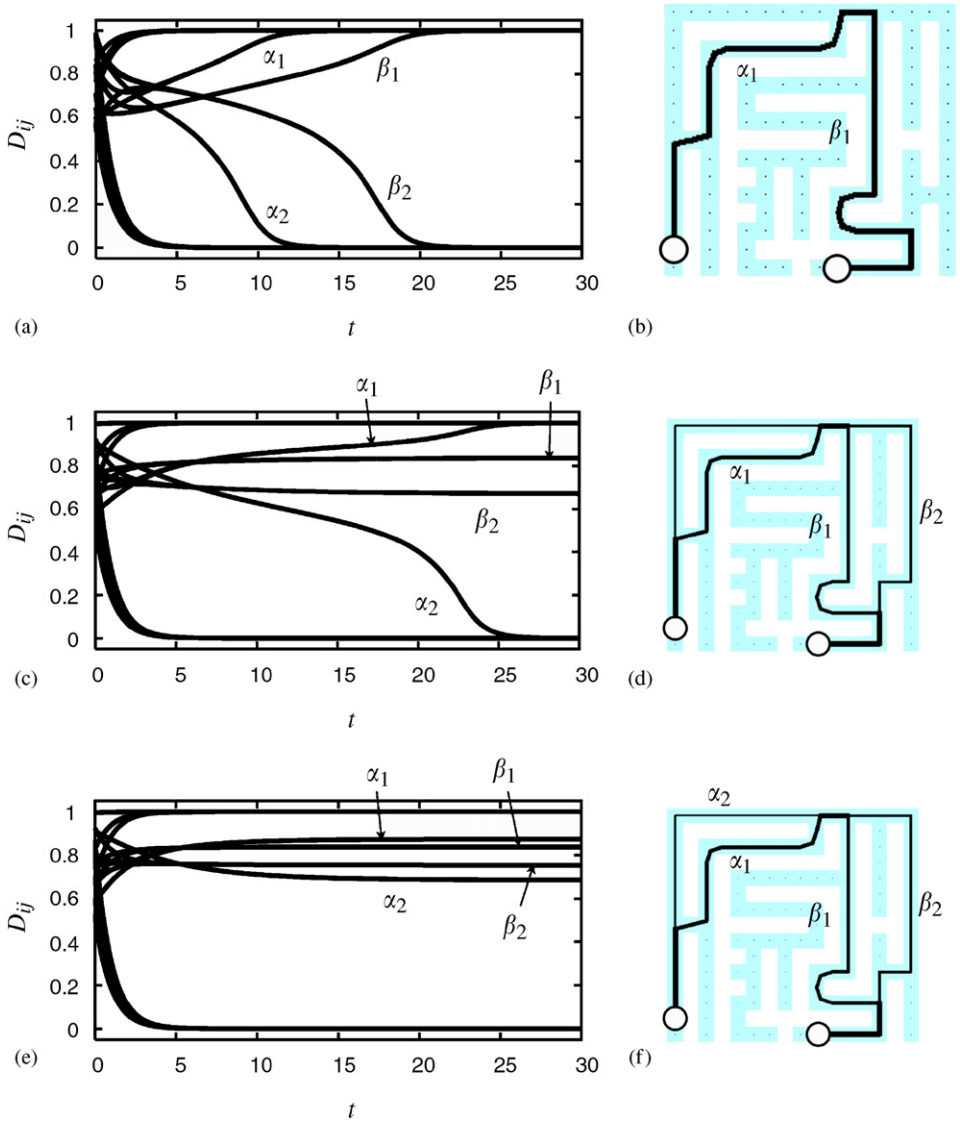

Fig. 10. The parameter is set at $\mu = 3.0$: (a) superimposed plots of D_{ij}'s vs. time for $a = 15.0$; (b) final state corresponding to panel (a); (c) superimposed plots of D_{ij}'s vs. time for $a = 22.0$; (d) final state corresponding to panel (c); (e) superimposed plots of D_{ij}'s vs. time for $a = 27.0$; (f) final state corresponding to panel (e).

set smaller than the one of β_2. Note that the path α_2 can also survive instead of α_1 if its initial conductivity is sufficiently larger than the one of α_1.

By comparing Figs. 5 and 6, it can be observed that the choice between competing paths is made more rapidly for larger values of μ. However, the basin of attraction to the shortest path (combination of paths α_1 and β_1) becomes narrower as μ goes larger, which were confirmed by a lot of simulations. Generally, the selection of the final path is dependent on the initial state in the parameter region $\mu > 1$, and any pair of the four possible combinations of paths remain stable to small perturbations.

Case II: $0 < \mu < 1$. In this parameter range, the final state is quite different from that of the previous case. All of the paths α_1, α_2, β_1, and β_2 survive at the end, as indicated in Figs. 7 and 8. Also, a large number of simulations have confirmed that the final state is the same, regardless of the initial state. Comparing the final conductivities of parallel paths such as α_1 and α_2, it is found that the shorter path finally achieves higher conductivity. Thus, the path β_1 attains higher conductivity than β_2 although the difference is smaller than the difference in conductivities of α_1 and α_2, as shown in Fig. 7(a).

If the parameter μ is taken as smaller, the convergence to the final state is more rapid, and the differences between the conductivities of the parallel paths are smaller than in the case shown in Fig. 7.

Case III: $\mu = 1$. This special value of μ makes $f(Q)$ linear and leads to results that are somewhat different from the previous cases, while the dead end cutting process is exactly the same. Fig. 9(b) shows that the shortest path is selected as the final state. Although it looks similar to the result of the case where $\mu > 1$, there are essential differences. In this case, the final state does not depend on the initial state,

which means that the shortest path always survives whether the distribution of conductivities in the initial state is random or biased. Furthermore, Fig. 9(a) shows that selection of the paths α_1, α_2, β_1 and β_2 is slower than in the previous cases.

4.2. Type II: $f(Q) = (1+a)Q^{\mu}/1 + aQ^{\mu}$

Here we examine how the asymptotic behavior varies corresponding to the change of the parameter a in Type II function. For smaller values of a the situation is similar to the case of Type I, $\mu > 1$, where only one of the competing paths remains, as shown in Fig. 10(a) and (b). On the other hand, Fig. 10(e) and (f) shows that all the competing paths can survive with larger values of a. For intermediate values of a, the result is also intermediate: only one of the pair α_1 and α_2 survives, while both of the pair β_1 and β_2 remain, as indicated in Fig. 10(c) and (d).

The Type II function with sigmoidal profile was motivated by the observation that the plasmodium makes many thinner tubes rather than a single very thick tube when the total sol flux is strong (corresponds to larger I_0, thus to larger a), while only a small number of tubes are retained when the sol flux is weak.

5. Simple graphs and analysis

In the previous section we observed a rich variety of network behavior that is not easy to analyse in a general form. In this section, we concentrate on graphs that are simple enough to permit of mathematical analysis but can still provide broadly applicable insights.

5.1. T-shaped graph

In both experiments and simulations of maze solving, rapid dead end cutting is always observed at the very outset. In order to demonstrate this property more clearly, we performed an experiment in which T-shaped initial tubes were prepared and food was supplied at the left and lower ends. The tubes in the upper branch then disappeared quickly, as shown in Fig. 11(a) and (b).

We used the graph in Fig. 11(c) to reproduce this experimental outcome. In this simple example, $Q_{13} = Q_{32} = 1$ and $Q_{34} = 0$, regardless of the form of the function $f(Q)$. Thus, D_{34} vanishes exponentially, while D_{13} and D_{32} converge to $f(1) = 1$. The conductivity of the dead end path vanishes exponentially because there is no flux in it at any time. In the general graph, the dead end path also vanishes exponentially for the same reason.

5.2. Ring-shaped graph—Type I: $f(Q) = Q^{\mu}$

We studied cases in which two paths connecting the same nodes compete, as indicated by the ring-shaped graph (Fig. 12). The corresponding graph consists of two nodes, N_1 and N_2, and two edges connecting them. For simplicity, we hereafter replace L^i_{12}, Q^i_{12}, and D^i_{12} $(i = 1, 2)$ by L_i, Q_i, and D_i, respectively. The fluxes along each path are calculated as

$$Q_1 = \frac{D_1/L_1}{D_1/L_1 + D_2/L_2} \quad \text{and} \quad Q_2 = \frac{D_2/L_2}{D_1/L_1 + D_2/L_2}. \tag{7}$$

Since Q_1 and Q_2 are nonnegative, adaptation equation (5) becomes

$$\begin{cases} \dfrac{\mathrm{d}}{\mathrm{d}t}D_1 = f(Q_1) - D_1, \\ \dfrac{\mathrm{d}}{\mathrm{d}t}D_2 = f(Q_2) - D_2. \end{cases} \tag{8}$$

We analyse the equation for the function form $f(Q) = Q^{\mu}$ $(\mu > 0)$ in this section. It is clear that there are three equilibrium points for equation system (8). Two of them describe the situation in which only one of the two paths survives and the other vanishes, and are given by $(D_1, D_2) = (1, 0)$ and $(0, 1)$. We name these equilibrium points A_1 and A_2, respectively. The third is the equilibrium point

$$(D_1, D_2) = \left(\left[\frac{1}{1 + (L_1/L_2)^{1/1-\mu}} \right]^{\mu}, \left[\frac{1}{1 + (L_2/L_1)^{1/1-\mu}} \right]^{\mu} \right),$$

which implies that both of the paths remain, and is named B. Simulations are performed by controlling the

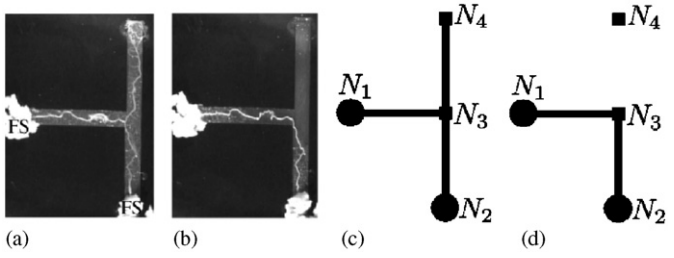

Fig. 11. Panels (a) and (b) indicate the initial and final states, respectively, of the T-shaped graph experiment. Panels (c) and (d) show, respectively, the initial and the final state of the simulation, which consisted of four nodes and three edges. The width of the black lines reflects the conductivity of each path.

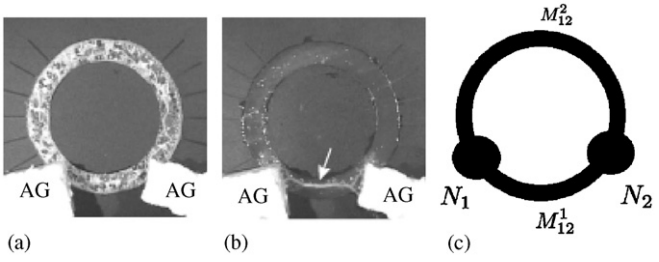

Fig. 12. Panels (a) and (b) indicate the initial and final state, respectively, of the ring-shaped network experiment. The lengths of longer and shorter paths are 42 and 13 mm, respectively. The corresponding graph is shown in panel (c), which has two nodes, N_1 and N_2, and two edges, M^1_{12} and M^2_{12}.

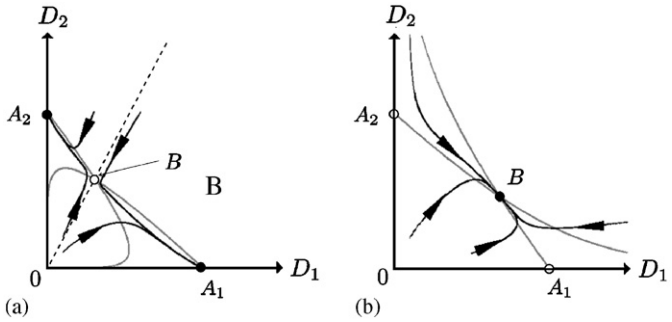

Fig. 13. Black curves with arrows indicate the orbit, and grey curves are null clines. The solid circle defines a stable equilibrium point and the open circle indicates an unstable equilibrium point. (a) The parameters are set at $\mu = 1.2$, $L_1 = 1.0$, and $L_2 = 1.1$. The dashed line given by $D_1/D_2 = (L_1/L_2)^{\mu/\mu-1}$ is a separatrix of the equilibria A_1 and A_2 which passes through B. (b) The parameters are set at $\mu = 0.8$, $L_1 = 1.0$, and $L_2 = 1.1$.

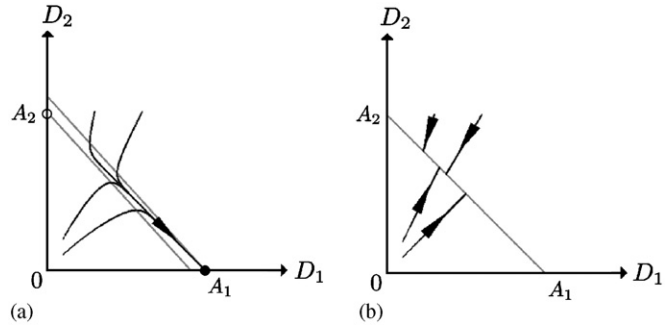

Fig. 14. Black curves with arrows indicate orbits and grey curves represent null clines. The solid circle indicates a stable equilibrium point, and the open circle indicates an unstable equilibrium point. (a) The parameters are set at $\mu = 1.0$ and $L_1 = 1.0$, $L_2 = 1.1$. Every orbit converges to the equilibrium point A_1. (b) The parameters are set at $\mu = 1.0$ and $L_1 = L_2 = 1.0$.

parameters μ, L_1, L_2 and the initial values, and we concentrate on the asymptotic behavior of the solution.

- $\mu > 1$. Fig. 13(a) shows several orbits in the D_1–D_2 phase plane. Each orbit converges to one of the two equilibria A_1 and A_2 and the initial values determine which one is attained in the final state. Tubes of greater length and lower conductivity, which characterize the initial state, tend to disappear. To be precise, the tube which has a greater value of $D_i^{\mu-1}/L_i^{\mu}$ in the initial state is the one that ultimately survives.
- $\mu < 1$. In this case, both of the tubes invariably survive, whatever the initial conditions. The final state is given by the equilibrium point B, as shown in Fig. 13(b).
- $\mu = 1$. The behavior of the solution for $L_1 = L_2$ differs from the solution for $L_1 \neq L_2$, as described below.

  (i) $L_1 \neq L_2$. There are two equilibria, A_1 and A_2, as indicated in Fig. 14(a). If $L_1 < L_2$ holds, the final state is always A_1, which means that the shorter tube survives regardless of initial values. If $L_1 > L_2$, every orbit converges to A_2 since the Eq. (8) is symmetric for exchanging the indices 1 and 2. In any case, only the shorter edge survives as long as $\mu = 1$.

  (ii) $L_1 = L_2$. Fig. 14(b) presents the results of the simulation. In this special case, all points on the line segment A_1A_2 are equilibrium points. It is easily observed that the ratio of D_1 and D_2 remains constant along each orbit. Therefore, the final state is given by the intersection of the line connecting the initial point and the origin with the line segment A_1A_2.

Let us summarize the simulation results in the following table:

		Equilibrium points	Final state	Dependence on the initial data
$\mu > 1$		A_1, A_2, B	A_1 or A_2	Exists
$\mu < 1$		A_1, A_2, B	B	None
	$L_1 < L_2$	A_1, A_2	A_1	None
$\mu = 1$	$L_1 > L_2$	A_1, A_2	A_2	None
	$L_1 = L_2$	$\overline{A_1A_2}$	Some point of $\overline{A_1A_2}$	Exists

We present a linear stability analysis at the equilibrium points in the various cases listed in the above table. The Jacobi matrix J on the right-hand side of Eq. (8) is calculated as

$$J = \begin{pmatrix} \mu Q_1^{\mu-1} \dfrac{D_2/L_2}{L_1(D_1/L_1 + D_2/L_2)^2} - 1 & -\mu Q_1^{\mu-1} \dfrac{D_1/L_1}{L_2(D_1/L_1 + D_2/L_2)^2} \\ -\mu Q_2^{\mu-1} \dfrac{D_2/L_2}{L_1(D_1/L_1 + D_2/L_2)^2} & \mu Q_2^{\mu-1} \dfrac{D_1/L_1}{L_2(D_1/L_1 + D_2/L_2)^2} - 1 \end{pmatrix},$$

and the Jacobi matrices at each equilibrium point are denoted $J(A_1)$, $J(A_2)$, and $J(B)$, respectively. We first examine the stability of the equilibrium point B. After some calculation, the following formula is obtained

$$J(B) = \begin{pmatrix} \mu Q_2^* - 1 & -\mu \dfrac{L_1}{L_2} Q_1^* \\ -\mu \dfrac{L_2}{L_1} Q_2^* & \mu Q_1^* - 1 \end{pmatrix},$$

where Q_1^* and Q_2^* are fluxes along the first and second tubes at the equilibrium point B. Using the relation $Q_1^* + Q_2^* = 1$, we have

$$\det J(B) = 1 - \mu \quad \text{and} \quad \operatorname{tr} J(B) = \mu - 2$$

thus,

$$\det J(B) < 0 \quad \text{for } \mu > 1,$$

$$\det J(B) > 0, \quad \operatorname{tr} J(B) < 0 \quad \text{for } 0 < \mu < 1.$$

This means that the equilibrium point B is a saddle (and thus unstable) for $\mu > 1$ and stable for $0 < \mu < 1$.

Next we analyse the stability of the equilibrium points A_1 and A_2. When $\mu > 1$,

$$J(A_1) = \begin{pmatrix} -1 & -\mu\dfrac{L_1}{L_2} \\ 0 & -1 \end{pmatrix}, \quad J(A_2) = \begin{pmatrix} -1 & 0 \\ -\mu\dfrac{L_2}{L_1} & -1 \end{pmatrix},$$

hence A_1 and A_2 are stable. When $0 < \mu < 1$, the right-hand-side of the equation system (8) is not differentiable at the equilibrium points A_1 and A_2. However, it is clear that the flow on the phase plane is severely repulsive around A_1 and A_2, and hence they are unstable. Together with the stability analysis of the equilibrium point B, these results support the simulation results shown in Fig. 13. When $\mu = 1$ and $L_1 \neq L_2$,

$$J(A_1) = \begin{pmatrix} -1 & -\dfrac{L_1}{L_2} \\ 0 & \dfrac{L_1}{L_2} - 1 \end{pmatrix}, \quad J(A_2) = \begin{pmatrix} \dfrac{L_2}{L_1} - 1 & 0 \\ -\dfrac{L_2}{L_1} & -1 \end{pmatrix}.$$

Therefore, A_1 is stable and A_2 is unstable when $L_1 < L_2$, and A_1 is unstable and A_2 is stable when $L_1 > L_2$ which agrees with the simulation results in Fig. 14.

5.3. Ring-shaped graph—Type II: $f(Q) = (1 + a)Q^{\mu}/1 + aQ^{\mu}$

In the maze solving simulations, we have already observed a different type of asymptotic behavior for the Type II function from the one of Type I. Let us analyse here how the asymptotic behavior depends on the parameter a. As in the Type I case, there are two equilibrium points, A_1 and A_2 which are given by $(D_1, D_2) = (1, 0)$ and $(0, 1)$, respectively. There is also another equilibrium point, B, as shown in Fig. 15(a), located closer to A_2 than to A_1 due to the asymmetry of L_1 and L_2. The two equilibria A_1 and A_2 are stable, while B is unstable. When the parameter a is increased, the saddle-node bifurcation occurs at some critical value of a^c, producing the stable equilibrium point C_1 and the unstable equilibrium point C_2. Thus, we have three stable equilibrium points, A_1, A_2, and C_1 for $a > a^c$, as indicated in Fig. 15(b). The convergence to the equilibrium point C_1 implies the coexistence of both edges in the final state, which does not occur for smaller values of a. As seen in panel (b), A_1 and A_2 can also be final states if the initial state is sufficiently biased. In contrast to the Type I case, it is difficult to obtain the expression of the coordinates of the points B, C_1 and C_2, and is also difficult to calculate the critical value a_c.

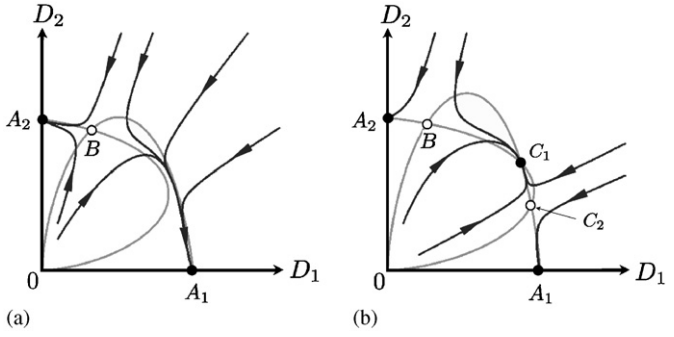

Fig. 15. The black curves with arrows indicate the orbits, and the gray curves are null clines. The solid circle indicates a stable equilibrium point and the open circle an unstable equilibrium point. The parameters were set at $\mu = 3.0$, $L_1 = 1.0$, and $L_2 = 1.1$ in both panels: (a) $a = 20.0$; (b) $a = 27.0$. The critical value of a is numerically obtained as $a_c = 24.73$.

6. Discussion

In this paper, we have described a simple mathematical model of the adaptive network of a plasmodium capable of solving a complex maze. The key underlying mechanism in the model is positive feedback: greater conductivity results in greater flux, and this in turn increases conductivity. As shown in the previous sections, the system evolves through the following two steps:

1. Dead end cutting.
2. Selection of the *solution* path from the competitive paths.

The basis of selection depends on the function form and parameter values.

From the point of view of maze solving, it is helpful to adopt a Type I function form with larger values of μ (> 1), if one wishes to reach a solution as *quickly* as possible, ignoring all possibilities of achieving alternative solutions. The choice of $\mu = 1$ as the Type I function is, in a sense, a special case. As we have shown, convergence is slower than with the other possible choices, but the shortest path can be derived without any concern for initial values. Therefore, there is a trade-off between speed and safety when the Type I function model is used to find the shortest path to a goal. On the other hand, the aim is to derive all possible paths connecting the starting point and the goal, it is useful to apply a Type I function with a smaller value of μ ($0 < \mu < 1$).

Our simulations strongly suggest that the convexity of the function $f(Q)$ essentially affects the asymptotic behavior of the system in the case of the Type I function. Although the analysis described above was confined to very simple graphs, a mathematical analysis of general conformation graphs is now underway. For the Type II function, we did not observe a clear relationship between the saddle-node bifurcation and the local convexity of the sigmoidal profile.

We used the sigmoidal function for a flux-conductance relationship as a more realistic form than the power function. The observation that there is a maximum tube diameter clearly motivates that the growth function should saturate, whatever the mechanism causing the saturation. This observation makes the functional form of the type II growth function a reasonable modification from the power-law growth function. We assumed that the flux was

proportional to the pressure difference, but the thixotropy (a property of non-Newtonian fluid) of protoplasm meant that it barely flowed when the pressure difference was small. Modeling the complex rheology of the protoplasm is beyond the scope of this paper. To account for this observation in our model, we take $\mu > 1$ in the type II growth law so that the growth is less sensitive to changes in the flux when the pressure differences are small.

The sigmoidal curve has physiological implications. The control of the organism's body shape in response to volume of available food follows a previously established rule: the number of remaining paths is larger when less food is provided to a fixed amount of plasmodial inoculum (see Nakagaki et al., 2001 for details). This behavior is considered trade-off between the physiological requirements of moving towards the FSs in order to consume the food and connecting the two FSs to maintain intracellular communication. When the given amount of food is small, only a small amount of plasmodium covers the food and more plasmodium is devoted to making connections, which makes the total flux of sol larger. Our simulation with the sigmoidal function could realize the situation in which multiple paths remain for a larger total flux. We therefore conclude that the sigmoidal relationship between sol flux and tube thickness explains the intelligent control of amoeboid behavior in *Physarum*.

We discuss a physiological role of contraction oscillations in path finding in *Physarum*. A portion of organism on a FS is regarded as one oscillator (referred to hereafter as an FS-oscillator) because it oscillates with sufficient synchrony. The flux flowing out from the source node depends on pressure difference between the two FS-oscillators, which is given by amplitudes and phases of the oscillators. One FS-oscillator is perturbed by the other as the sol flow mediates physical and chemical interactions between the two FS-oscillators (Oster and Odell, 1984; Teplov et al., 1991; Tero et al., 2005). This therefore represent a system of coupled oscillators with variable interaction. What is then required is for the coupled oscillator dynamics to be solved together with the adaptive network dynamics. However, it is acceptable to ignore the coupled oscillator dynamics in cases of two FSs, because sol flows back and forth between the two FSs, irrespective of the phase difference shown by the oscillators. The time-scale for adaptive process of tube thickness is much shorter than that of shuttle flow. It is reasonable to assume that the shuttle flow rate is averaged over an oscillation period and that a model takes the form of direct current. In fact, we confirmed that the simulation results were essentially the same if we replaced the total flux by $\cos \omega t$, where ω gives the shorter time-scale than that of adaptation.

By contrast, when the number of FSs is larger than three, one must include the coupled oscillator dynamics, because the network dynamics cannot be decoupled from the dynamics of the pressure oscillations at the FSs. Therefore, the next stage is to write down the oscillator dynamics, with the aim of reproducing them in mathematical models of networks containing multiple FSs, as demonstrated in our previous studies (Nakagaki et al., 2004a,b). The tube network of true slime mold is a nice experimental system for studying the self-organization of adaptive transportation networks in nature.

The model proposed in this paper suggests how the true slime mold solves a problem to complete a task necessary for its survival. The dynamic behaviors of the plasmodium, simulated in our model, can be regarded as a means of information processing in the absence of a nervous system. A positive feedback mechanism between the conductance of sol flow (or tube thickness) and sol flow plays a key role. It remains unclear how this feedback mechanism is realized at the material level of the protoplasmic sol and gel. However, it is possible to conclude that such a system does not require a central processing unit, but that parallel dynamics within each part of the protoplasm are sufficient for its information processing requirements. The algorithm of slime mold for problem solving is of particular interest when considering the evolutionary origin of information processing by the brain. *Physarum* is a useful model system for studying the emergence of information processing in physical terms and its tube network helps to explain how the self-organization of adaptive transportation networks develops in nature.

Acknowledgments

We are grateful to Professor J. Keener for critical discussion and helpful suggestion. RK is supported by Grant-in-aid for Scientific Research NO. 16654017 of the Japan Society for the Promotion of Science. TN is supported by Grant-in-aid for Scientific Research NO. 15300098 of the Japan Society for the Promotion of Science.

References

Kamiya, N., 1959. Protoplasmic streaming. Protoplasmatologia 8, 1–199.

Matsumoto, K., Ueda, T., Kobatake, Y., 1988. Reversal of thermotaxis with oscillatory stimulation in the plasmodium of *Physarum polycephalum*. J. Theor. Biol. 131, 175–182.

Miyake, Y., Tabata, S., Murakami, H., Yano, M., Shimizu, H., 1996. Environment-dependent self organization of positional information held in chemotaxis of *Physarum* plasmodium. J. Theor. Biol. 178, 341–353.

Nakagaki, T., Yamada, H., Tóth, A., 2000a. Maze-solving by an amoeboid organism. Nature 407, 470.

Nakagaki, T., Yamada, H., Ueda, T., 2000b. Interaction between cell shape and contraction pattern. Biophys. Chem. 84, 195–204.

Nakagaki, T., 2001. Smart behavior of true slime mold in labyrinth. Res. Microbiol. 152, 767–770.

Nakagaki, T., Yamada, H., Tóth, A., 2001. Path finding by tube morphogenesis in an amoeboid organism. Biophys. Chem. 92, 47–52.

Nakagaki, T., Yamada, H., Hara, M., 2004a. Smart network solution by an amoeboid organism. Biophys. Chem. 107, 1–5.

Nakagaki, T., Kobayashi, R., Nishiura, Y., Ueda, T., 2004b. Obtaining multiple separate food sources: behavioural intelligence in the *Physarum* plasmodium. Proc. R. Soc. London Ser. B 271, 2305–2310.

Nagai, R., Yoshimoto, Y., Kamiya, N., 1978. Cyclic production of tension force in the plasmodial strand of *Physarum polycephalum* and its relation to microfilament morphology. J. Cell Sci. 33, 205–225.

Naib-Majani, W., Stockem, W., Wohlfarth-Bottermann, K.E., 1982. Immunocytochemistry of acellular slime mold *Physarum polycephalum*. II. Spatial organization of cytoplasmic actin. Eur. J. Cell Biol. 28, 103–114.

Oster, G.F., Odell, G.M., 1984. Mechanics of cytogels I: oscillations in *Physarum*. Cell Motility 4, 469–503.

Stockem, W., Brix, K., 1994. Analysis of microfilament organization and contractile activities in *Physarum*. Int. Rev. Cytol. 149, 145–215.

Takahashi, K., Uchida, G., Hu, Z.-S., Tsuchiya, Y., 1997. Entrainment of the self-sustained oscillation in a *Physarum polycephalum* strand as a one-dimensionally coupled oscillator system. J. Theor. Biol. 184, 105–110.

Takamatsu, A., Tanaka, R., Yamada, H., Nakagaki, T., Fujii, T., Endo, I., 2001. Spatio-temporal symmetry in rings of coupled biological oscillators of *Physarum Plasmodium*. Phys. Rev. Lett. 87, 078102, 1–4.

Teplov, V.A., Romanovsky, Yu.M., Latushkin, O.A., 1991. A continuum model of contraction waves and protoplasm streaming in strands of *Physarum polycephalum*. Biosystems 24, 269–289.

Tero, A., Kobayashi, R., Nakagaki, T., 2005. A coupled-oscillator model with a conservation law for the rhythmic amoeboid movements of plasmodial slime molds. Physica D 205, 125–135.